Synthesis, spectroscopic, and computational studies on molecular charge-transfer complex of 2-((2-hydroxybenzylidene) amino)-2-(hydroxymethyl) propane-1, 3-diol with chloranilic acid: Potential antiviral activity simulation of CT-complex against SARS-CoV-2

Tarek E. Khalil*, Hemmat A. Elbadawy, Asmaa A. Attia, Doaa S. El-Sayed

Chemistry Department, Faculty of Science, Alexandria University, 2 Bagdad Street, P.O. Box 2-Moharrem Beck, Alexandria 21321, Egypt

ARTICLE INFO

ABSTRACT

An innovative charge-transfer complex between the Schiff base 2-((2-hydroxybenzylidene) amino)-2-(hydroxymethyl) propane-1,3-diol [SAL-THAM] and the π-acceptor, chloranilic acid (CLA) within the mole ratio (1:1) was synthesized and characterized aiming to investigate its electronic transition spectra in acetonitrile (ACN), methanol (MeOH) and ethanol (EtOH) solutions. Applying Job's method in the three solvents supported the 1:1 (CLA: SAL-THAM) mole ratio complex formation. The formation of stable CT-complex was shown by the highest values of charge-transfer complex formation constants, K_{CT}, calculated using minimum-maximum absorbance method, with the sequence, acetonitrile > ethanol > methanol

DFT study on the synthesized CT complex was applied based on the B3LYP method to evaluate the optimized structure and extract geometrical and reactivity parameters. Based on TD-DFT theory, the electronic properties, ^{1}H and ^{13}C NMR, IR, and UV-Vis spectra of the studied system in different solvents showing good agreement with the experimental studies. MEP map described the possibility of hydrogen bonding and charge transfer in the studied system. Finally, a computational approach for screening the antiviral activity of CT - complex towards SARS-CoV-2 coronavirus protease via molecular docking simulation was conducted and confirmed with molecular dynamic (MD) simulation.

1. Introduction

Schiff's bases are important for the production of special chemicals like bioactive heterocycles, pharmaceuticals, rubber additives, and amino protective groups in organic synthesis. Schiff's bases are of great importance in analytical, liquid crystals, polymer chemistry, dyes, pigments, catalysts, and intermediates in organic synthesis, and polymer stabilizers [1–4]. They have a wide range of biological activities, including antibacterial, antifungal, antiviral properties [5,6].

Another remarkable compound is chloranillic acid (CLA), a versatile class of organic compounds known as benzoquinones. CLA has a specific electronic structure and properties responsible for its widely used in synthesizing charge transfer complexes [7]. CT interaction between electron donors containing oxygen, nitrogen, or sulfur atoms and electron acceptors, such as benzoquinones, is important for many physical properties of materials, including electrical, conductivity, magnetic, and optical properties [8–10]. Also, it plays a significant role in various fields as the drug receptors binding mechanism, solar energy storage, surface chemistry, and many biological systems [11–13]. Many charge transfer receptors have been discussed in terms of the hydrogen bonding approach [14].

Although the comprehensive studies carried out on charge transfer complexes between nitrogenated compounds and electron acceptors, there still many compounds whose charge transfer complexes have not been reported yet.

COVID 19 is officially named severe acute respiratory syndrome coronavirus 2 (SARS-CoV-2), where this virus is the infective mediator of the in-progress pandemic of coronavirus disease 2019 (COVID-19) [15–18]. CoVs are present in four types, α-, β-, δ- and γ-coronaviruses [19]. SARS-CoV-2 is a member of β-coronaviruses, Robson [20] defined SARS-CoV-2 viral protein as a strain of human SARS [21].

Many ideas have been offered in the direction of facing the Corona pandemic, including drug repurposing, drug combination, and design drug models. Many approved medications have been tested against SARS-CoV-2 using large-scale in-silico and in-vitro studies, as well as molecular docking [22–25]. Virtual screening is a great tool for suggesting potential medications. Out of 48 antiviral medicines evaluated, Sangeun Jeon et al. found 24 probable SARS-CoV-2 antiviral medication candidates. Some therapeutic candidates had very low 50% inhibitory concentrations (IC50 [48]), including two FDA-approved medicines, niclosamide and ciclesonide [22]. Employing advanced virtual screening to repurpose 6218 approved and clinical trial drugs for COVID-19. Seven of the evaluated drugs were able to inhibit SARS-CoV-2 growth in Vero cells. Emodin, omipalisib, and tipifarnib had anti-SARS-CoV-2 action in Calu-3 human lung cells. In Calu-3, omipalisib was 200 times more active than remdesivir. The synergistic effects of (remdesivir/omipalisib) and (tipifarnib/omipalisib) on SARS-CoV-2 were demonstrated, showing better efficiency [25]. Recent in-silico molecular docking studies improved the utilization of several medications such as remdesivir and mycophenolic acid acyl glucuronide as possible candidate therapeutics for treating COVID-19 [24].

Design drug models is also a well-known method to predict the potential drug activity before biomedical testing, using molecular simulation and parameters evaluation to inhibit or decrease the viral activity by investigating the active binding sites, which could help shorten the time and reduce effort and cost [26–29].

The main protease (M^{pro}) and the paplian-like protease (PL^{pro}) are responsible for the processing of viral polyproteins yielding mature viral proteins [30,31]. Current relative work was established to explain the possible use of protease inhibitors as a treatment against infections of SARS-CoV-2. Computational features and molecular screening compromise new testable assumptions for effective drugs involved for novel coronavirus [29,32]; GC-376 is a 3C-like protease (3CL^{pro} or M^{pro}) inhibitor that can stop the activation of functional viral proteins essential for replication and transcription in host cells. Recently, it was used to check inhibition of SARS-Cov-2 M^{pro} in vitro, and the outcomes display potent inhibition of this target. These data recommend that GC-376 and its metabolites may have therapeutic potential for Covid-19 [33].

In the current study, we aim to (1) Synthesis of a novel charge transfer complex derived from the previously prepared THAM-SAL Schiff's base [34] and chloranilic acid (CLA), (2) Investigate the behavior of the new prepared CT complex in different polar solvents as ethanol, methanol, and acetonitrile using UV–Vis absorption spectra, (3) Study the influence of increasing the concentration of the electron donor on the formed CT-complex and deducing its formation constants in the three solvents. (4) Apply computational studies; (a) to determine the stabilization energy for the formed CT complex as well as its geometrical parameters (bond lengths and bond angles) using PCM as solvation model for energy minimization together with TD-DFT (b) presenting the molecular potential energy surface, as well as the HOMO and LUMO molecular orbitals of the produced complex, (c) visualizing non-covalent interaction (NCI) in the molecules, and (d) The antiviral activity of CT - complex against SARS-CoV-2 coronavirus protease with the target of COVID-19 protease enzymes was demonstrated utilizing DFT and molecular docking simulation.

2. Materials and methods

2.1. Materials and instrumentation

All the chemicals utilized were of analytical quality. Spectroscopic grade methanol (MeOH), ethanol (EtOH), and acetonitrile (ACN) as well as Chloranilic acid [CLA], and (2,5-dichloro-3,6-dihydroxy-1,4-benzoquinone), with purity ($\geq$ 98%) were obtained from Sigma-Aldrich. Salicylaldehyde and Tris(hydroxymethyl)aminomethane, THAM were obtained from Across Organics. A Perkin-Elmer FTIR Spectrophotometer-FTIR1650 was used to measure FT-IR spectra in the 400–4000 cm^{-1} range, and the samples were prepared as KBr discs. A double beam spectrometer, UV–Vis (T80 + UV/Vis), PG Instruments Ltd, UK, was utilized to estimate the electronic absorption spectra over a wavelength range of 350–700 nm.

2.2. Synthesis of the CT-complex [SAL-THAM-CLA]

The solid CT complex is prepared as follow:

(1) Synthesis of Schiff's base [*SAL-THAM*] derived from salicylaldehyde and Tris-(hydroxymethyl)aminomethane, THAM, as previously described [34].
(2) Addition of 1.25 mmol of ethanolic solution of CLA (0.0261 g, in 25 mL of EtOH) to 1.25 mmol of [SAL-THAM] (0.0281 g, in 25 mL of EtOH), and applying reflux for 3 h at 80°C.
(3) The solution was allowed to gently evaporate at room temperature, yielding a pink solid. The pink crystals were filtered off, washed multiple times with EtOH, then using diethyl ether, and finally dried in a vacuum desiccator for 24 h over anhydrous CaCl$_2$. Using methanol or acetonitrile as solvents, the identical complex was obtained.

[SAL-THAM-CLA] Yield: (79.58%); M.W. 434.22 g mol^{-1}; m.p. = 177 °C). Elemental analysis, found: C, 47.16; H, 3.79; N, 3.48%; Calculated for $C_{17}H_{17}Cl_2NO_8$: C, 47.02; H, 3.95; N, 3.23%. IR: ν (cm^{-1}); 3417 (m), 3240 (m), 1620 (s), 1520 (s), 1504(s), 1373(s), 1265(s), 1165(s), 1056(s),825 (s), 700 (w). ^{1}H NMR (DMSO-d^6): δ_H 7.67 (CH, benzene), 5.24 (broad, OH, alcohol), 3.47, 2.49 (CH$_2$, methylene) ppm. ^{13}C NMR (DMSO-d^6): δ_C 39.50, 59.28, 60, 96 and 104.67 ppm.

2.3. Preparation of THAM-Schiff's base and CLA standard solutions

SAL-THAM Schiff's base and CLA fresh standard stock solutions of 1.0×10^{-3} mol L^{-1}, were prepared by dissolving an accurate weight of each in the applicable volume of solvent (EtOH, MeOH, and ACN). The proper volumes of the donor and acceptor stock solutions were mixed, and then the solvent was added to complete the solution for spectroscopic measurements.

2.4. Studying the formation constants of the CT-complex (KCT)

The formation constants (K$_{CT}$), were estimated using the minimum-maximum absorbance method [35] consistent with the following method. A series of 10 mL calibrated measuring flasks were filled with two milliliters of CLA stock solution (1.0×10^{-3} mol L^{-1}). To each of these flasks, different volumes of a freshly prepared stock SAL-THAM solution (1.0×10^{-3} mol L^{-1}) were added and diluted to the mark with ethanol, methanol, or acetonitrile.

The lowest concentration of SAL-THAM made a minimum absorbance of the complex (A$_{min}$). The donor's concentration is steadily increased, and the CT- complex absorbance is recorded (A$_{mix}$) until the greatest constant absorbance (A$_{max}$) is achieved.

The following formula was used to obtain the CT-formation constants (K_{CT})

$K_{CT} = (A_{mix}-A_{min})/[(A_{max}-A_{mix})C]$ where A_{max} is the maximum absorbance of the formed CT-complex, A_{min} is the minimum absorbance of the CT-complex, A_{mix} represents the absorbance values of the mixture that lies between A_{max} and A_{min}, and C is the concentration of the added SAL-THAM in mol L^{-1} [35].

2.5. Density functional theory (DFT) study

Density functional theory (DFT) calculations of the reactants and product were performed using Gaussian 09 w [36] software. The geometries of the reactants and product were fully optimized at B3LYP/6–311 G (d,p) basis set [37]. Gauss View 6.0 was used to construct the molecular structure input files and visualize the optimized structures. Geometrical and reactivity parameters were calculated after optimization. Proton nuclear magnetic resonance (HNMR) was performed using density functional theory/gage-including atomic orbital (DFT/GIAO) approach. IR spectra for all reactants and products were calculated. The electronic properties were discussed based on UV–Vis spectra obtained by the TD-DFT method using the PCM model [38,39] in different solvents (methanol, ethanol, and acetonitrile). Molecular electrostatic potential (MEP) explained the total charge density on the surface of the studied system to demonstrate the transfer of charge from the donor to the acceptor part in the titled structure.

2.6. Molecular docking simulation

Due to the vital role of charge transfer in site inhibition and biological control [40], molecular docking studies have been performed after geometry optimization of the studied CT complex. Protein molecular target SARS-CoV-2 main protease (M^{pro} and PL^{pro}) was obtained from the Protein Data Bank (PDB) (www.rcsb.org) with four genome species 6WTT, 6XA4, 6XBH, and 7JRN. A molecular docking investigation was implemented using a validated AutoDock 4.2 software [41]. In the initial step, the protein target was prepared to remove any water molecules, ions, and small ligands; also, the reference ligand in the binding comparison was removed from the grid space considering the location of its binding amino acids. Assignment of Gasteiger charges to the molecular docking system. Addition of polar hydrogen to the protein receptor due to its significant binding effect. CT ligand was imported to investigate its docking behavior and a grid box was formed to initiate the docking run through the auto grid platform using selected dimensions with a grid size of 64×120×40 with spacing 0.375 Å. The docking process was run with the genetic algorithm of 50 runs applying a population size of 300. The number of GA evaluations was 250,000. The free binding energy with the lowest cluster evaluation seems to be the best docking conformation. USCF Chimera1.13.1 [42] was utilized to perform molecular dynamic simulation analysis, discovery studio software (http://www.accelrys.com) was utilized for some visualizations.

3. Results and discussion

3.1. Synthesis and characterization

The (1:1) molar ratios reaction between Schiff base [SAL-THAM] and CLA in ethanol is expected to achieve through either a charge transfer complex with H-bond formation (I) or H-bond formation together with proton transfer (II), as shown in Scheme 1.

3.2. Fourier- transform infrared (FT-IR)

The study of FT-IR spectroscopic properties is based on a comparison for the essential band locations between the electron
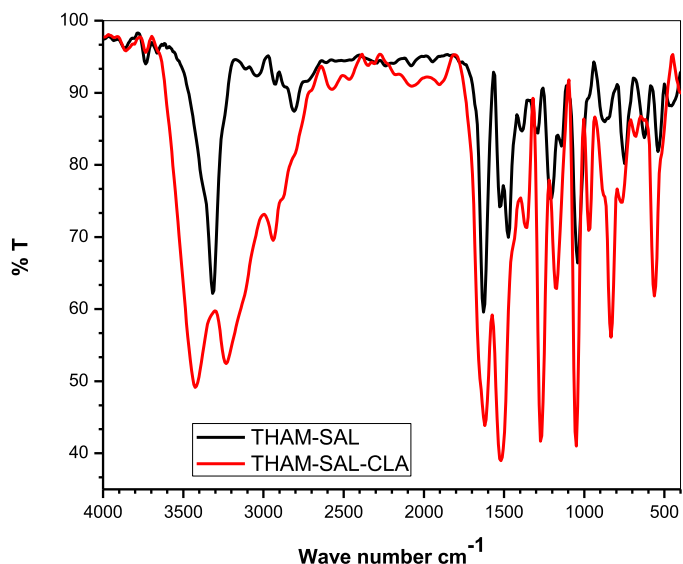

Fig. 1. KBr disk FT-IR spectra of SAL-THAM and CT complex [SAL-THAM-CLA].

donor Schiff base [SAL-THAM], the electron acceptor "Chloranilic acid" [CLA], and the formed CT-complex [SAL-THAM-CLA]. The following are the significant differences in band frequencies and intensities in the FTIR spectra of the produced CT-complex, Fig. 1, when compared to its reactants:

1. The significant band of azomethine group $\nu(C = N)$, which appeared in SLA-THAM at 1628(s) cm^{-1}was red-shifted and appeared at 1620 cm^{-1}in the CT-complex, indicating that the azomethine nitrogen has changed its nature with a new character in the new compound.
2. The carbonyl group of CLA$\nu(C=O)$ at 1664 and 1631 cm^{-1}appeared as only one band at 1620 cm^{-1}in the CT-complex, which overlapped with the band corresponding to the azomethine group, with a shoulder at 1651cm^{-1}.
3. The stretching vibration of the hydroxyl group $\nu(OH)$ of CLA appeared at 3235and 3317 cm^{-1}, while in the spectra of the SAL-THAM, a sharp band at 3315 cm^{-1} and a shoulder at 3394 cm^{-1} were identified. In case of [SAL-THAM-CLA], two new bands appeared at 3425 and 3234 cm^{-1} which may attribute to $\nu(OH)$ and protonation of the azomethine nitrogen of SAL-THAM, respectively. This observation strongly supported the probability of the presence of both charge transfer as well as a proton transfer hydrogen-bond between the OH of CLA and the azomethine nitrogen of THAM-SAL as shown in Scheme 1 (II).
4. The bands at 847 and 745 cm^{-1} characteristics for the $\nu(C–Cl)$ in CLA are shifted 832 and 765 cm^{-1} in the spectrum of the CT complex, indicating charge migration from the donor to the acceptor to form a 1:1 CT complex. Finally, the FT-IR spectra confirm the presence of both proton transfer and charge transfer in the CT complex.

However, the IR spectra of the CT complex have been performed in the three solvents (MeOH, EtOH and ACN) and the representative figure was displayed in the supplementary data as **Fig. S1.** The solution IR spectra in the three solvents showed similar behavior, with slightly shifted peaks that may be attributed to the solvent effects and in agreement with UV–Vis results. In ACN, new band appeared at ca. 3230 cm^{-1} which may due the protonation of the azomethine nitrogen of SAL-THAM.
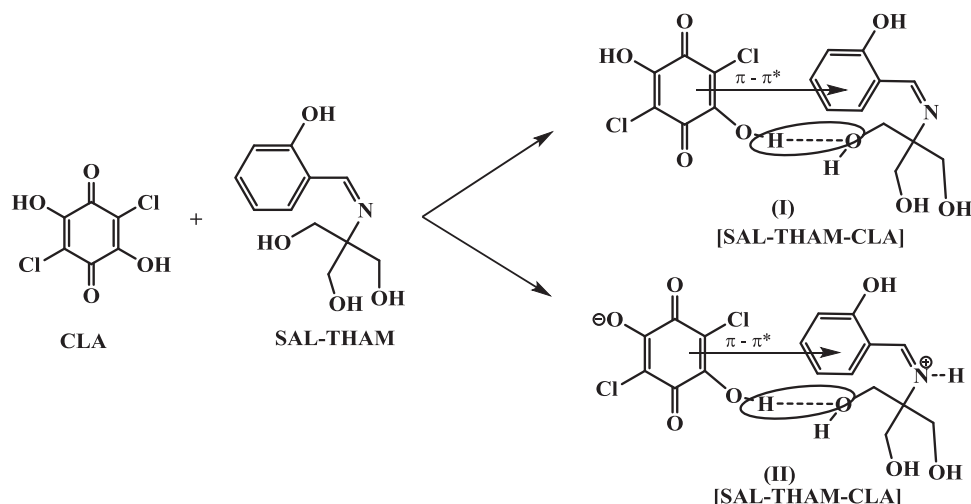
Scheme 1. 2D graphical representation of proposed structure for charge transfer complex [SAL-THAM-CLA]. (I) H-bond complex structure and (II) mixed H-bond with proton transfer complex structure.
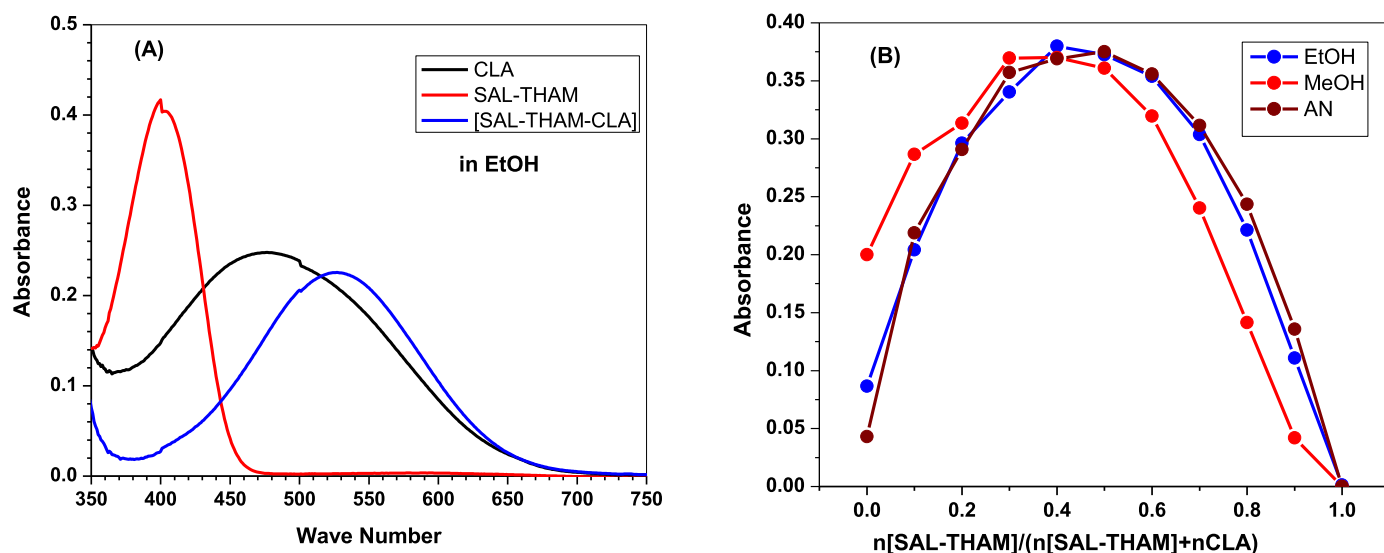

Fig. 2. (A) UV- vis absorption spectra of 2×10^{-4} M of the free donor (SAL-THAM), free acceptor (CLA) and CT complex of [SAL-THAM-CLA] in ethanol; (B) Continues variations method (Job's method) at room temperature of the formed CT complex [SAL-THAM-CLA] in methanol, ethanol, and acetonitrile.

3.3. Electronic absorption spectra

3.3.1. UV–Vis absorption spectral of the CT complex

In ethanol, methanol, and acetonitrile solutions at room temperature, UV–Vis absorption spectra of the free donor (SAL-THAM) Schiff's base, the free acceptor (CLA) and the prepared charge transfer complex are recorded. Fig. 2A shows the spectral data in EtOH; the spectra of CT-complex reveal a notable strong absorption band centered at *ca.*524, 520, and 514 nm in ethanol, methanol, and acetonitrile, respectively. These bands are related to a dramatic color difference noticed after mixing the reactants, illustrating electronic transitions in the produced CT-complexes in the visible region. It can be noticed that the charge transfer band was red-shifted in the position from 524 nm or 520 nm in protic solvents, EtOH or MeOH, respectively, to 514 nm in the aprotic solvent, acetonitrile, indicating that the CT-complex formation's high sensitivity to the polarity of the used solvent.

3.3.2. Molecular composition of the produced CT complex

The continuous variation Job's approach was used to estimate the molecular composition of the produced CT-complex in the dif-

ferent three solvents at room temperature [43]. Fig. 2B expresses the continuous variant plots of donor/acceptor molar ratios, like ethanol, methanol, or acetonitrile solutions. The formation of only 1:1 CT-complex is confirmed by the spectral characteristics. As a result, it is concluded that the polarity of solvents has no effect on the molecular composition of the complex in solutions.

3.3.3. Concentration effect of reactant on CT complex formation

By measuring the absorbance of the generated CT-complex in ethanol, methanol, and acetonitrile, the effect of increasing the SAL-THAM concentration, which is the e-donor, in the presence of a constant concentration of the e-acceptor (CLA) was investigated, Fig. 3. It is found that, in all solvents, the absorbance of the formed CT-complex increases as the donor concentration increase at the same λ_{max} of the CT complex, signifying the creation of a stable CT- complex in the used solvent.

3.3.4. Influence of time on the formation of CT-complex

The influence of time upon the formation of CT-complex was investigated by mixing 1.0×10^{-3} M from THAM-Schiff's base and CLA (1:1 molar ratio) in ethanol, methanol, and acetonitrile. The
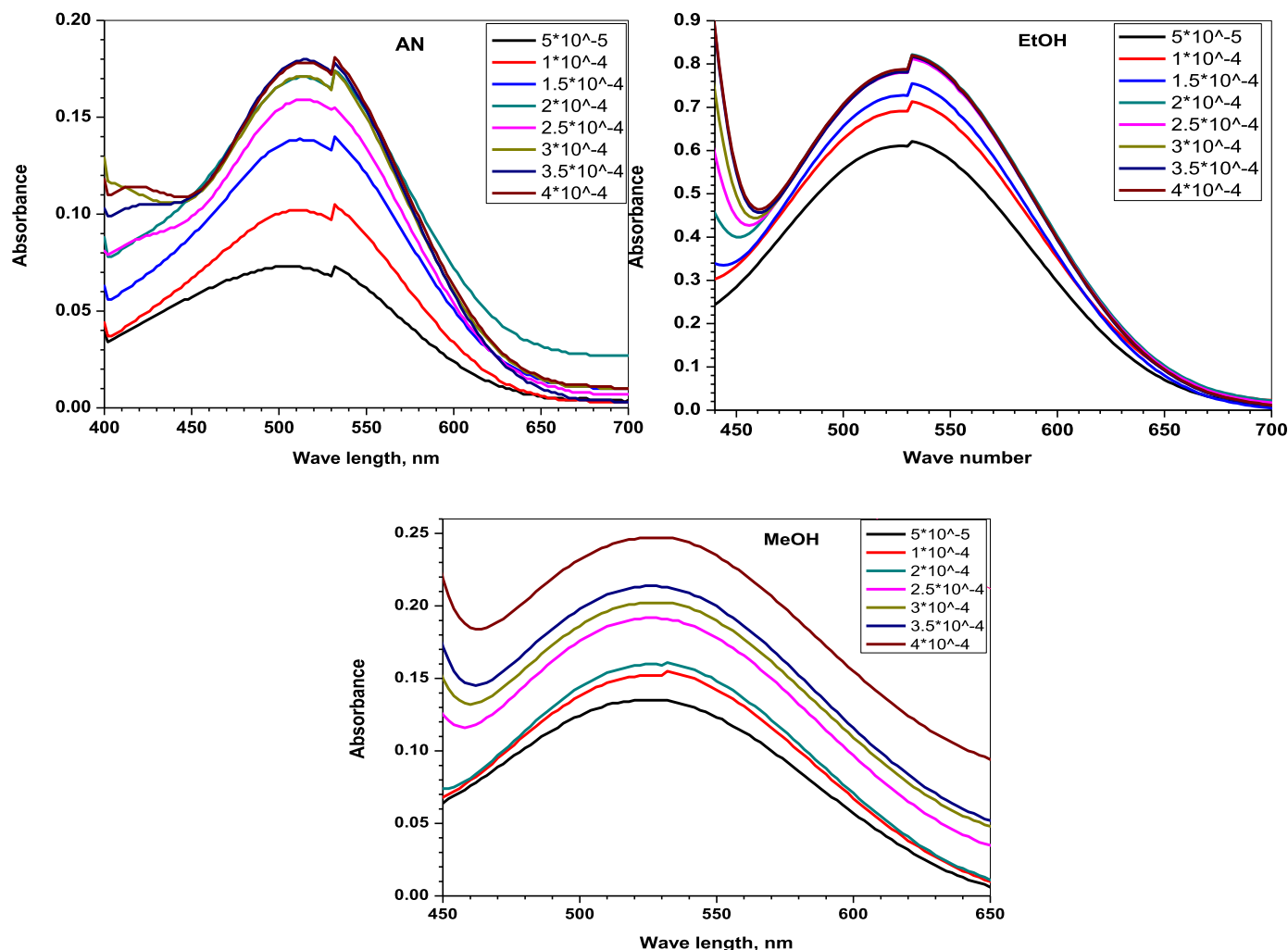
Fig. 3. Effect of concentration on the formed CT complex [2.0 × 10^{-4} mol/dm^3 CLA with various concentrations of SAL-THAM from 5.00×10^{-5} to 4.00×10^{-4} mol/dm^3] in methanol, ethanol, and acetonitrile, at room temperature.

absorbance of the generated CT-complex was found to be constant and maximal in all solvents tested, indicating that the complex's absorbance is time independent, Fig. S2. The CT-complex absorption value didn't vary throughout the course of the two-hour experiment; this confirms its stability which can be attributed to the strong bonding between CLA and THAM-Schiff's base moieties.

3.3.5. Formation constant (KCT) of the CT complex

K_{CT} values are estimated by applying the minimum-maximum absorbance method [35], based on the electronic spectra of the produced CT-complex at many concentrations of the donor in various solvents, and the results are gathered in Table 1. In general, high K_{CT} in all solvents support the formation of stable CT-complex. The data showed that the K_{CT} is strongly solvent dependent with the order: acetonitrile > ethanol > methanol, in which the smallest aprotic solvent from the solvent parameters view, acetonitrile, displays the highest formation constant value relative to the other protic solvents, methanol, and ethanol.

The variance in K_{CT} values from aprotic to protic solvents was illustrated according to the solvent parameters, Π* (dipolarity / polarizability) and electric permittivity of solvent (εT). The solvent small electric permittivity stabilized the complex ground state and consequently led to maximum approach between donor and acceptor species. In other words, it is greatly dependent on the hydro-

gen bond donor and acceptor parameters (α and β respectively) of the examined solvent [44]. Ethanol and methanol have high hydrogen bond donor values of 0.93 and 0.83, respectively. Thus hydrogen bonding contact between the hydroxyl group of ethanol or methanol and the SAL-THAM molecule is formed. The CT transit from the e - donor to the e-acceptor was significantly slowed by this interaction, resulting in the lowest K_{CT} in methanol. Because the α values in methanol are higher than those in ethanol, a stronger interaction when methanol is used. As a result, the stability constant of ethanol is much larger than that of methanol. Because ACN cannot prevent charge transfer from SAL-THAM to CLA via hydrogen bond formation, the stability constant for acetonitrile was larger than those for ethanol and methanol. Acetonitrile, on the other hand, has a high dielectric constant ε (37.5) and polarizability parameters π* (0.75), which promote charge transfer from donor to acceptor in the generated CT complex. Hence, as the polarity of the solvent increased in response to the increased contact between the dipole of the donor-acceptor link and acetonitrile, the formation constant is increased.

3.4. Computational methods

3.4.1. Geometry optimization

The optimized molecular structures of donor, acceptor, and the formed complex are presented in Fig. 4. The optimized complex

Table 1

Minimum-maximum absorbance data for CT complex formation K_{CT} of [SAL-THAM-CLA] at room temperature using; methanol, ethanol, and acetonitrile solvents.

Solvent	λ_{max} (nm)	Conc. SAL-THAM (mol/L)	A_{min}	A_{max}	$A_{complex}$	K_{CT} (L/mol)	Average K_{CT} (L/mol)
Methanol	520	0.00010	0.135	0.387	0.151	677.966	1068.65
		0.00015			0.159	701.754	
		0.00020			0.1591	526.315	
		0.00025			0.191	1142.85	
		0.00030			0.201	1182.79	
		0.00035			0.213	1280.78	
		0.00040			0.246	1968.08	
Ethanol	524	0.00010	0.610	0.826	0.690	5882.35	11,103.29
		0.00015			0.726	7733.33	
		0.00020			0.783	20,116.28	
		0.00025			0.778	14,000	
		0.00030			0.782	13,030.3	
		0.00035			0.780	10,559.01	
		0.00040			0.786	11,000	
		0.00045			0.771	6505.051	
Acetonitrile	514	0.00010	0.072	0.192	0.102	333.333	15,136.5
		0.00015			0.138	8148.148	
		0.00020			0.171	23,571.43	
		0.00025			0.159	10,545.45	
		0.00030			0.171	15,714.29	
		0.00035			0.18	25,714.29	
		0.00040			0.178	18,928.57	

molecular structure in the gas phase, Fig. 4(c), is stabilized by hydrogen bond formation via the oxygen of the THAM hydroxyl group and the hydroxyl group of the CLA part. Table S1 shows the geometrical parameters of the optimized structures CLA, SAL-THAM, and CT complex [SAL-THAM-CLA]. The optimized bond lengths of the reactants and the formed CT complex indicate the complex formation resulting from the hydrogen bond property.

Comparing the bond lengths and angles between the reactants and product showed the presence of inter-and intra-molecular hydrogen bonding in the product, as follows:

(1) Regarding CLA, bond length O(39)…H(43) has increased from 0.970 Å to 0.995 Å in the complex, while the other O…H bond length remained the same with 0.970 Å.
(2) The bond angle of C5-O10-H14 and C1-O9-H13 in CLA is increased from 109.0° to be 116.9° in the CT complex (C31-O39-H43)
(3) Concerning the SAL-THAM unit, upon complex formation, intramolecular hydrogen bond O23…H26 is formed with a length of 2.001 Å, and the C21-O27 is elongated from 1.428 Å to 1.535 Å. In addition, the bond angle of O39-H43-O27 becomes 134.5°
(4) The CT complex has a new intermolecular hydrogen bond between the two reactant units (O27…H43) with a length of 1.930 Å

3.4.2. Reactivity parameters

The reactivity parameters are calculated to explain various features of the examined charge transfer reaction. In gas phase and methanol, the highest occupied and lowest unoccupied molecular orbital (HOMO & LUMO) energies were determined for the studied optimal complex structure, [Scheme 1, (I) Fig. 4(c)].

Many reactivity parameters such as ionization potential (I), electron affinity (A), chemical potential (μ), chemical hardness (η), global chemical softness (σ) and energy fraction (X) are estimated from HOMO & LUMO values. The results are listed in Table 2, from which numerous characteristics of reactivity associated with chemical reactions can be estimated [45]. Table 2 shows the charge separation between atoms in gas phase and solution using total energy E (a.u.), nuclear repulsion energy NRE (Hartees), and dipole moment (D).

Table 2

Reactivity parameters of the complex in gas phase with B3LYP/6–311 g (d,p).

Parameter	Gas	Methanol
E	−2235.299	−2235.228
NRE	2945.693	2945.693
D	3.503	3.943
E_{HOMO}	−8.217	−7.619
E_{LUMO}	−5.251	−4.844
E_{GAP}	2.966	2.775
I	8.217	7.619
A	5.251	4.844
M	−6.734	−6.232
H	1.483	1.388
Σ	0.674	0.720
X	1.565	1.573

The following Eqs provide definitions for some parameters.

$$I = - E_{HOMO} \tag{1}$$
$$A = - E_{LUMO} \tag{2}$$
$$\eta = (I-A)/2 \tag{3}$$
$$\mu = - (I+A)/2 \tag{4}$$
$$\sigma = 1/\eta \tag{5}$$
$$E_{GAP} = E_{LUMO} - E_{HOMO} \tag{6}$$
$$X = E_{HOMO} / E_{LUMO} \tag{7}$$

Fig. 5 illustrates the electronic transition between HOMO and LUMO levels for each reactant molecule and the product in the gas phase. The energy gap of the product (2.966 ev) is less than that of reactants, signifying higher stability of complex I formation.

Studying the interaction between CLA and SAL-THAM units, two product structures may be expected, as demonstrated in Scheme 1. Structure I possess only hydrogen bonding between the two units, while Structure II has proton transfer in addition to hydrogen bonding. Applying the same method of calculations B3LYP/6–311 G (d,p) in the gas phase to evaluate the optimized structures, the total energies of CLA, SAL-THAM, system I, and Structure II were found be −1451.282, −784.021, −2235.299, and −2226.156 Hartee, respectively. As the difference in energy between reactants and product measures the stability of the product formed, the energy difference in the formation of structure I equals +0.004 Hartee (i.e. 10.502 kJ/mol). In contrast, in structure II, ΔE is +9.147 Hartee
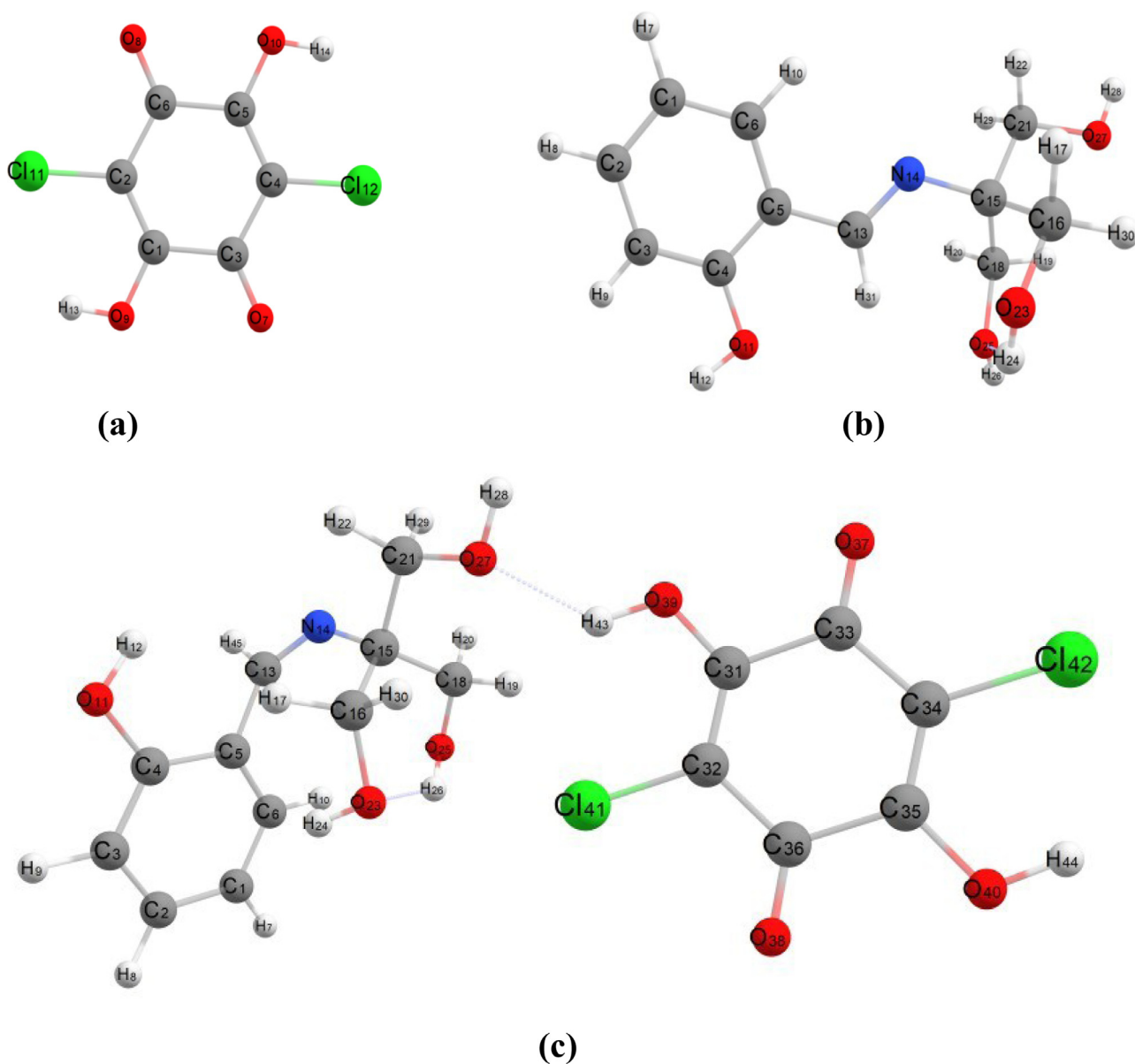
Fig. 4. The optimized (a) CLA (b) SAL-THAM (c) CT complex [SAL-THAM-CLA].

(i.e. 24,015.45 kJ/mol). Though the higher energy difference in the formation of structure II makes this path theoretically less favorable, its formation was found to be more accepted in practice (evidenced by the IR results). This may be attributed to the solution effect, especially by increasing the activation energy of reactants (inducing thermal energy) [46].

Fig. S3 shows the natural bond orbital (NBO) charge distribution of each atom of the reactants CLA, SAL-THAM, and product [CLA-SAL-THAM]. It was investigated that the reactive centers are represented in H of the hydroxyl group in the CLA part and O of the SAL-THAM part. To discuss the charged oxygen atoms in the reactant and the product, it was found that the charges on O23, O25, and O27 of the reactant are −0.749, −0.737, and −0.766, while the charges on O23, O25, and O27 of the product are found to be −0.756, −0.743 and −0.778 respectively. In case of CLA moiety of the product, the charge on H43 and H44 atoms have 0.517 and 0.483 on each one, respectively, while charges on H13 and H14 of CLA reactant have the same value (0.485). This means that in the CT complex, the charges of H atoms were directed to be more positive, and charges on O atoms were directed to be more negative.

Hence, the centers become more active towards charge transfer by H-bond formation.

3.4.3. IR, ^{1}H NMR, and ^{13}C NMR spectra

The CT complex, structure I, is confirmed by applying IR, ^{1}H NMR, and ^{13}C NMR at the same level of geometrical calculations (DFT/ B3LYP/6–311 G (d,p)). Fig. S4 shows the calculated IR spectra for the reactants and product. The peak corresponding to the OH group in the case of chloranilic molecule appeared at 3652 cm^{-1} showed a red-shift to 3574 cm^{-1}, upon charge transfer complexation, due to the intermolecular hydrogen bond formation.

Quantum chemical gage-independent atomic orbital (GIAO)-DFT NMR analysis was performed on the optimized structure. Fig. S5 presented the predicted ^{1}H NMR spectra for the low energy structure of the charge-transfer complex. The spectra showed an increase in the chemical shift of CLA–hydroxyl proton, H(43) to 7.436 ppm, while the other, H(44), appeared at 4.974 ppm. The different values are attributed to the various electronic environment surrounding each proton, confirming the intermolecular H bonding represented as O(39)…H(43)…O(27). In addition, estimation of the

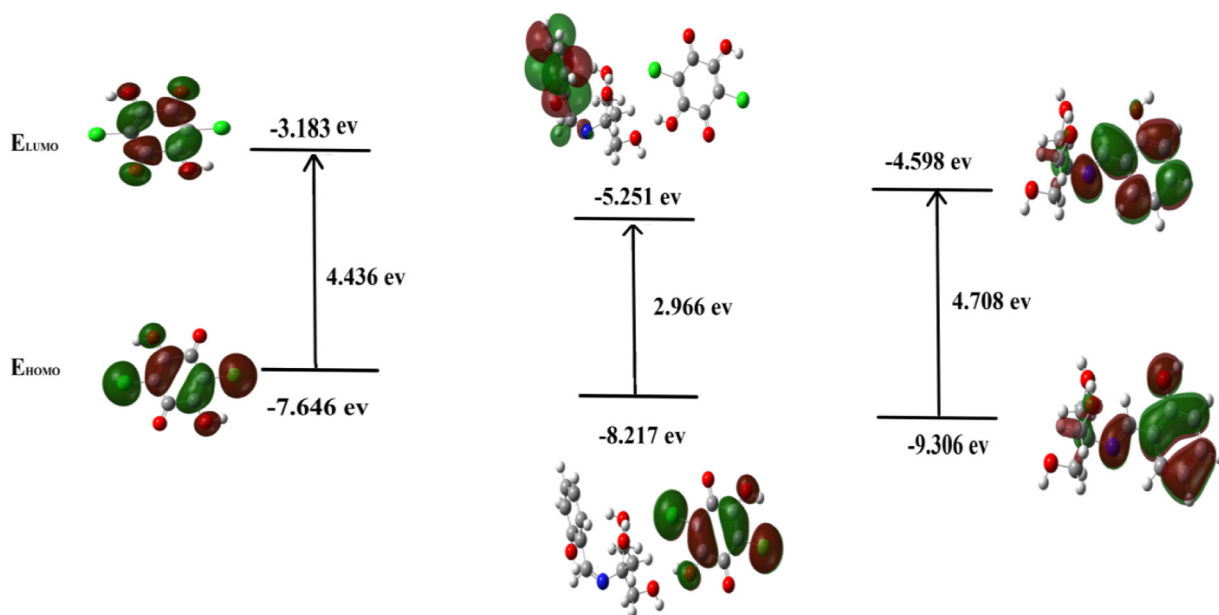**Fig. 5.** Molecular orbitals with their energy values for the optimized reactants and product in gas phase.
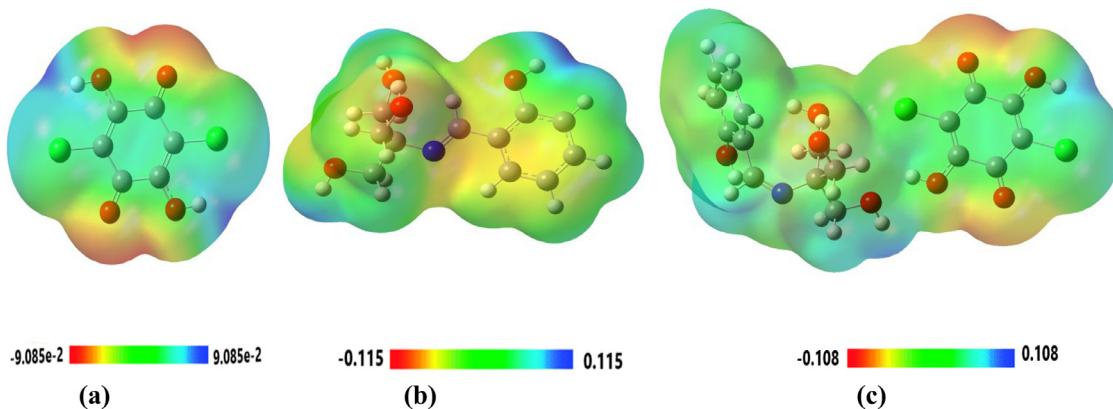

Fig. 6. MEP maps of a) CLA b) SAL-THAM and c) CT complex [CLA-SAL-THAM].
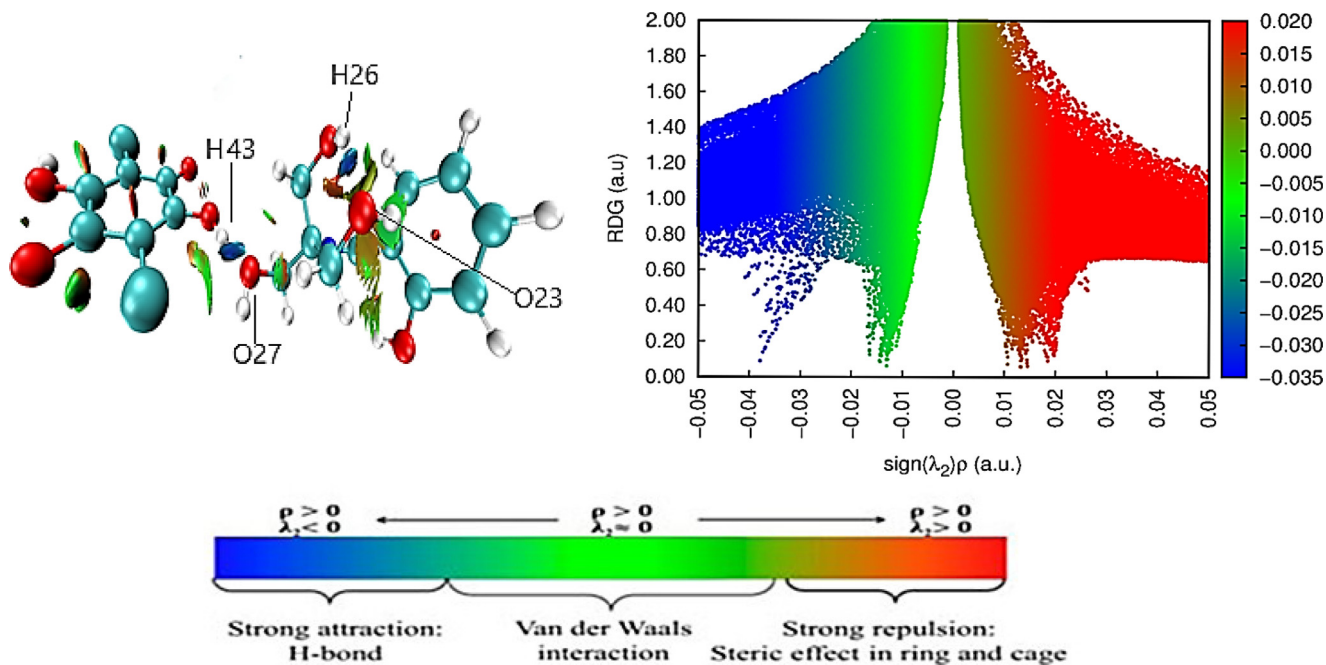

Fig. 7. RDG isosurface analysis and NCI scatter mapping diagram of the optimized CT complex.

type of carbon atoms is deduced via ^{13}C NMR spectral calculations, as shown in Fig. S6. The predicted spectroscopic NMR data of the studied complex I are summarized in Table S2. Generally, the calculated ^{13}C and ^{1}H NMR data are more or less identical with the experimental NMR results for the isolated CT complex [CLA-SAL-THAM], as shown in Fig. S7.

3.4.4. TD-DFT computations and origin of electronic spectra

The origin of electronic spectra of the complex (structure I) in different solvents has been computed using the TD-DFT/6–31 G (d,p) method via adding polarizable continuum solvation model PCM. The calculated electronic spectra of the complex in methanol, ethanol, and acetonitrile are shown in Fig. S8. The calculated electronic spectra in methanol, ethanol, and acetonitrile revealed broad bands at λ_{max} = 476 nm (oscillator strength 0.033), 481 nm (oscillator strength equal 0.024), and 464 nm (oscillator strength 0.029), respectively. The band is mainly assigned for HOMO-1 to LUMO in the three solvents with the contribution of 70.4%, 70.9%, and 72.5% for methanol, ethanol, and acetonitrile, respectively. It can be concluded that the electronic transition in the three solvents is of type π-π^{*} where the excitation of π-electrons involved the lower energetic orbital HOMO-1 and the higher energetic orbital LUMO. Compared with the experimental results, the shift in band positions may be due to the solvent effect and its behavior in solutions.

3.4.5. Molecular electrostatic potential analysis (MEP analysis)

MEP is an excellent approach that defines the distribution of electrostatic potential on the surface of a molecule. This can explore the electrophilic and nucleophilic attack regions and hydrogen bonding interaction. Fig. 6 illustrates MEP map of the studied system. There are different colors in the electrostatic potential:

Table 3

Free binding energy of reference and synthesized inhibitors with different protein receptors.

Protein ID	Reference inhibitor code	$\Delta G_{ref.inhibitor}$	$\Delta G_{CT-complex}$
6WTT	K36	−7.67	−5.65
6XA4	UXS	−9.59	−8.01
6XBH	ELL	−9.52	−3.17
7JRN	TTT	−8.92	−4.73

blue denotes the positive region, green denotes the neutral region, and red represents the negative region. Red color occurs on the THAM part of SAL-THAM Schiff base, confirming its contribution as hydrogen bond acceptor and acts as a nucleophile.

Concerning CLA molecule, one can notice the blue color on the OH groups considered H-bond donors and acts as an electrophile. On the other hand, for [CLA-SAL-THAM] complex, the disappearance of either the blue color in CLA or most of the red-orange color around THAM has been observed. This approves the charge transfer from the e-donor SAL-THAM part towards the e-acceptor CLA part.

3.4.6. Non-covalent interactions and reduced density gradient (NCI-RDG)analysis of CT complex surface

NCI-RDG profile analysis is substantial evidence of predicting different NCI strengths in other regions of the molecule. Interactions such as hydrogen bonding, van der Waals (VDW), and steric repulsive interactions are represented in mapped colored codes [47]. RDG iso surface visualization and NCI scattered graphical profile are illustrated in Fig. 7.

The color codes ranged from blue representing H-bond interaction; green code shows VDW interactions, and red code shows
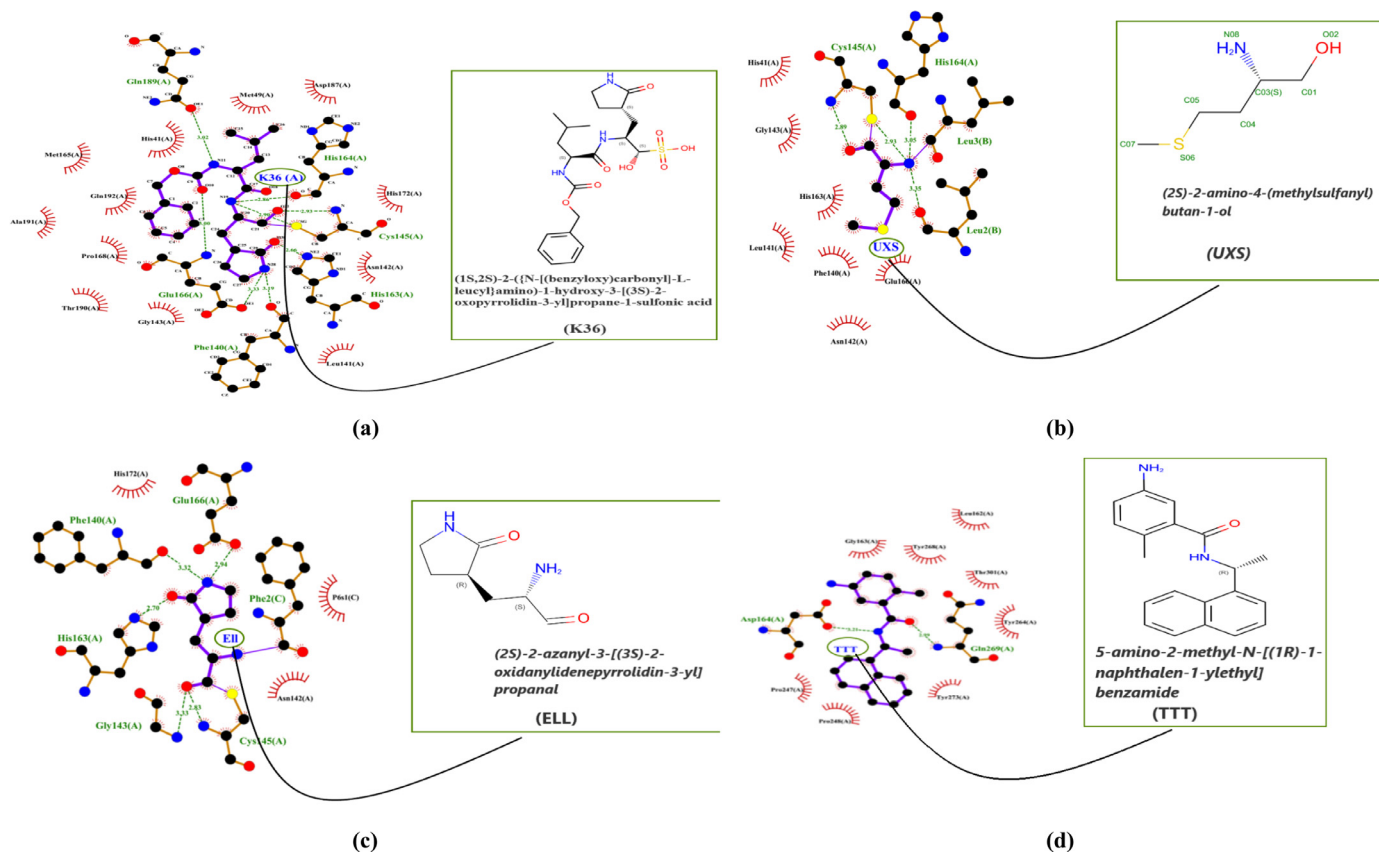

Fig. 8. 2D-interaction scheme of reference ligands complexed with SARS-CoV-2 protease enzyme (a) 6WTT (b) 6XA4 (c) 6XBH (d) 7JRN.
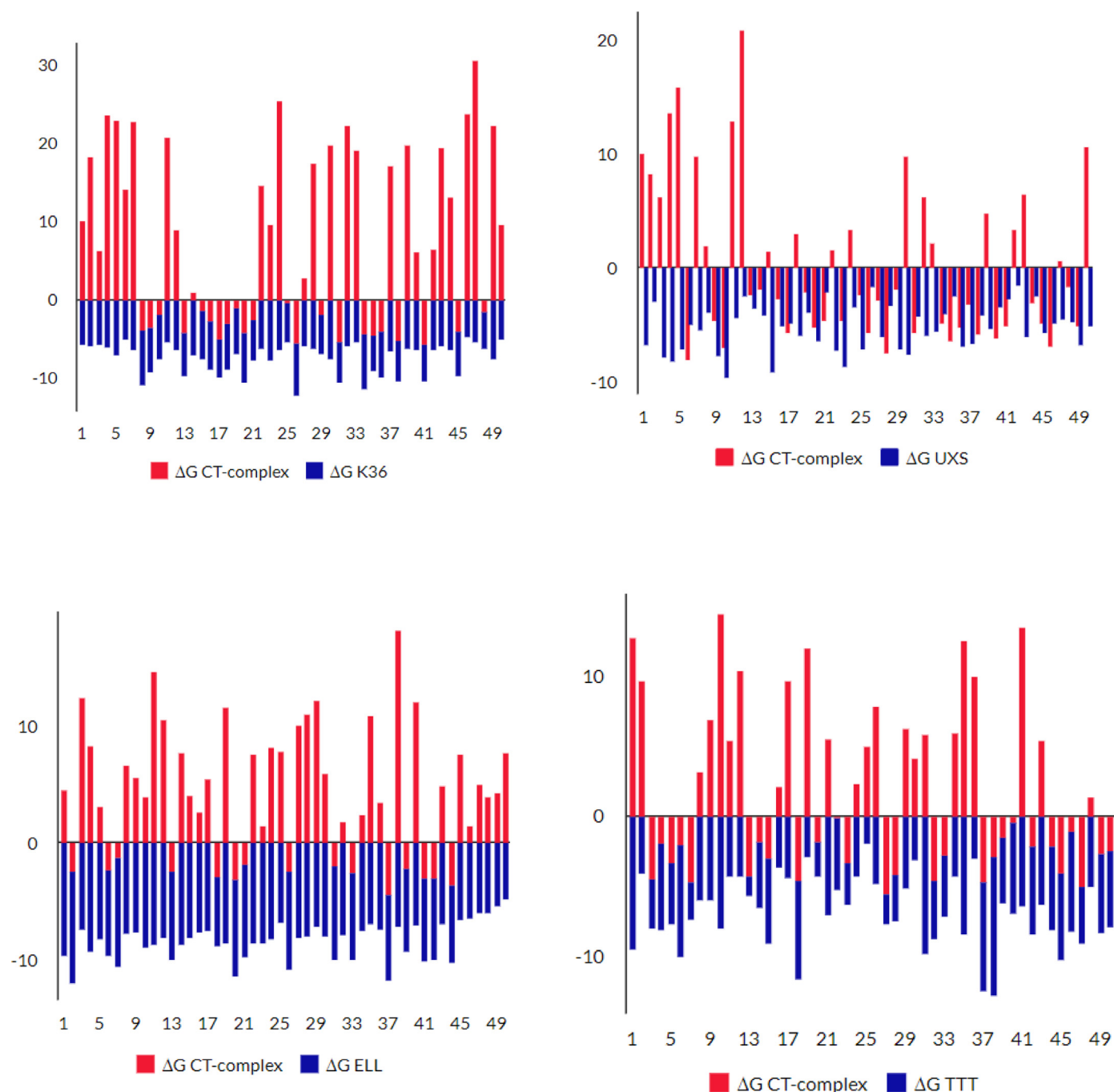
Fig. 9. Vertical bar representation the comparable free binding energies between the reference ligands and CT-complex (the blue bar in each figure corresponding to a specific reference ligand and the red bar represents binding affinity results of CT-complex with protein receptors).

repulsion interactions due to steric hindrance. The scatter mapping diagram measures the strength of these interactions. A high negative value represents strong H-bond formation and the gradient decreasing in this value, passing through weak H-bond and increasing the strength of VDW interaction to end with a significant positive value indicating the presence of strong repulsion interactions. So, the region between hydrogen (H43) of CLA moiety and oxygen (O27) of SAL-THAM is marked with blue color. Also, H-bond is formed between O23 and H26 of SAL-THAM.

3.4.7. Investigating CT-complex antiviral activity against SARS-CoV-2 protease

In-silico molecular docking of the studied synthesized CT complex was performed with the crystal structure of four viral protein type genomes with ID codes; 6WTT, 6XA4, 6XBH, and 7JRN. All viral crystal genomes were published in the recent year complexed with potential active drugs. Molecular docking simulation applied with the aid of previously approved ligands complexed to the chosen targets. GC-376 is an approved drug inhibitor for the main protease enzyme through a small k36 ligand. UAW241 and UAW247 are main protease inhibitors containing AUS (L-methioninol) and small ligand ELL as a unique ligand as a PDB [48].

Fig. 8 represents a graphic 2D-ligand-target interaction of K36, UXS, ELL, and TTT where K36 unique ligand is complexed with a target of 6WTT PDB code through blocking HIS164.A, CYS145.A, HIS163.A, PHE140.A, GLU166.A, and GLN189.A, active sites (Fig. 8a). UXS ligand is complexed with the target of 6XA4 PDB code through blocking HIS164.A, and CYS145.A (Fig. 8b). ELL ligand is com-
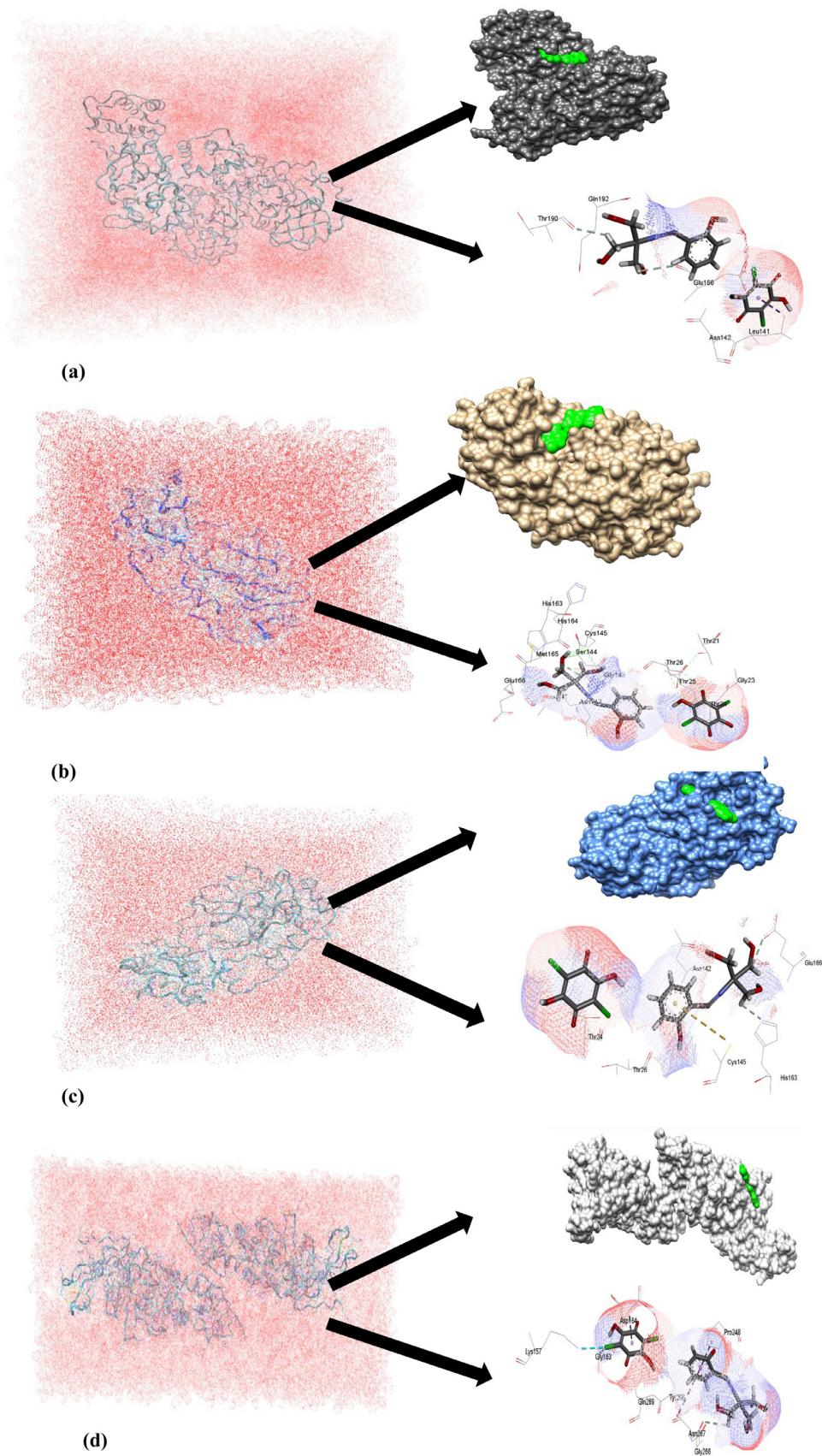
Fig. 10. Biomolecular solvated box grid including the interacting of CT-complex with active amino acids of (a) 6WTT, (b) 6XA4, (c) 6XBH and (d) 7JRN.
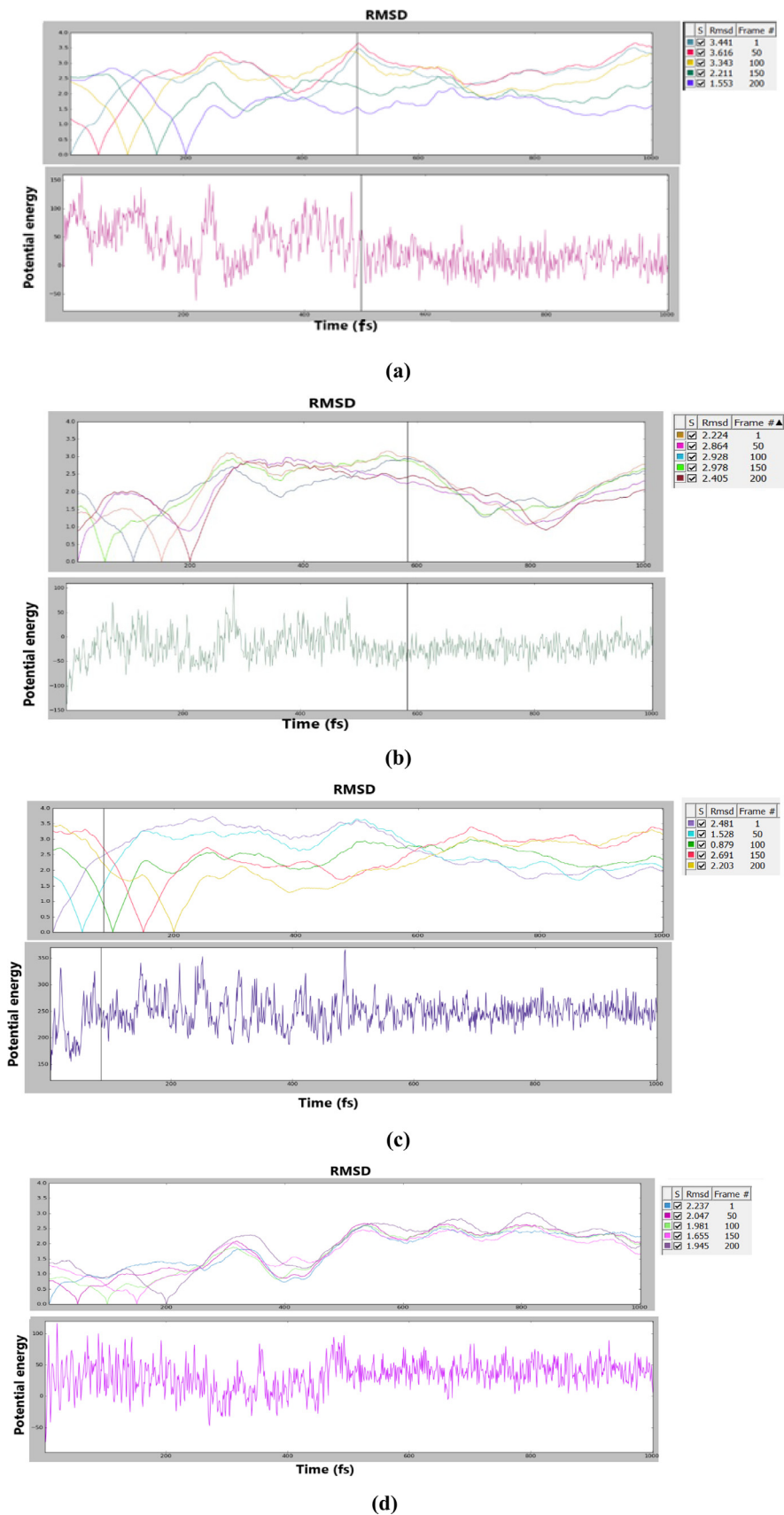
(a)

(b)

(c)

(d)

Fig. 11. MD simulation showing potential energy related to RMSD for CT-complex actively bound to (a) 6WTT, (b) 6XA4, (c) 6XBH and (d) 7JRN, active sites.
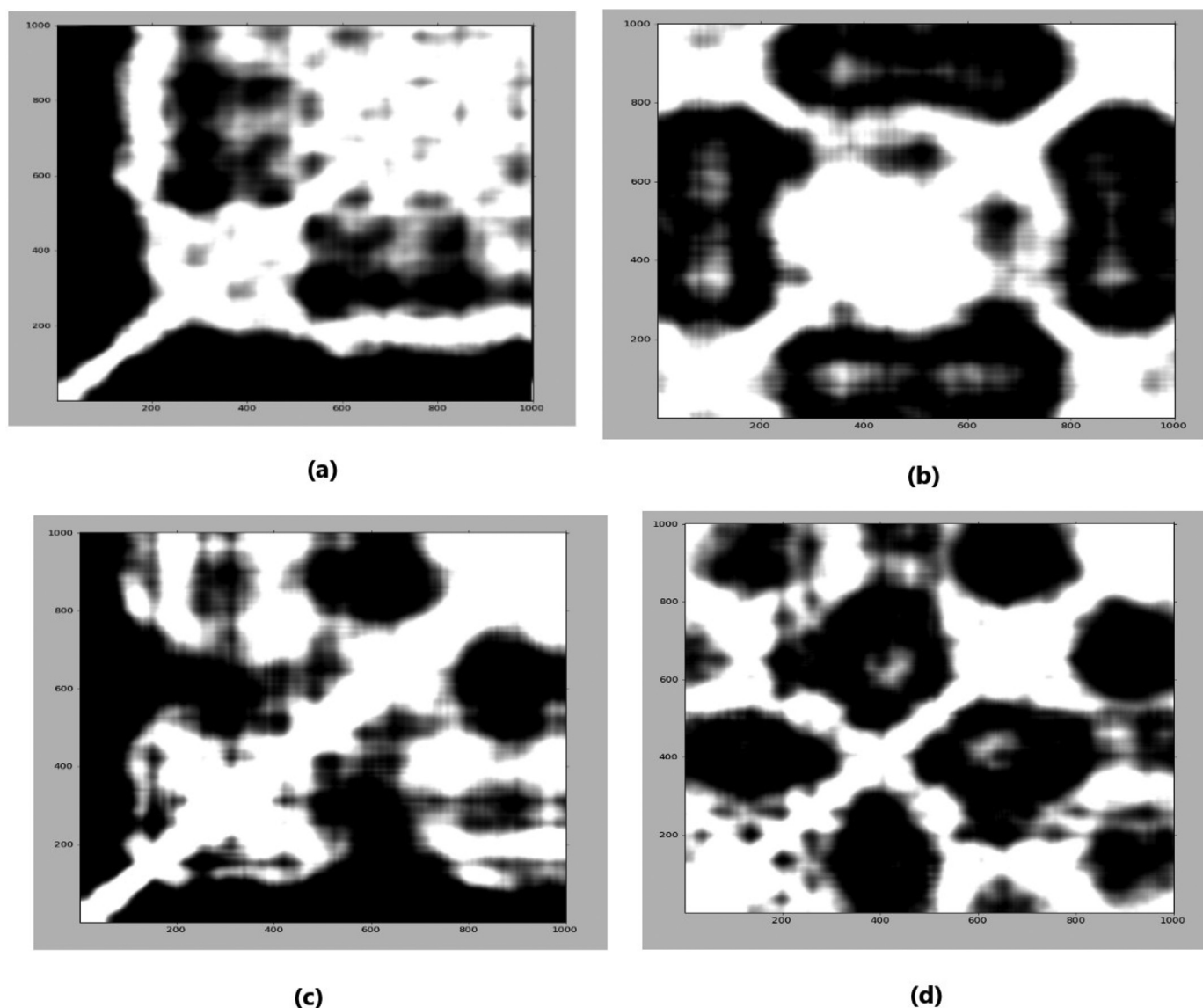
Fig. 12. 2D - RMSD map for binding of CT-complex with 6WTT **(a)**, 6XA4 **(b)**, 6 × 4BH **(c)** and 7JRN **(d)**; RMSD scanning range varies from 0.8Å-3.6 (white code area color corresponding to RMSD ⟨ 1.5 and black code colored area is corresponding to RMSD ⟩ 1.5).

plexed with the target of 6XBH PDB through blocking PHE140.A, GLU166.A, CYS145.A, GLY143.A and HIS163.A (Fig. 8c). TTT unique ligand is complexed with the target of 7JRN PDB through blocking ASP164.A and GLN269.A active sites (Fig. 8d).

3.4.8. Validation of molecular docking using AutoDock 4.2

Lamarckian Generic Algorithm (LGA) scoring function is the principal method for detecting the binding strength. The interactive relationship between the binding inhibitors and protein cleft can be compared with the free binding energy calculated, this is due to investigate the validity of docking visualization results based on the SARS-CoV-2 reference inhibitors present in the crystal structure of the desirable protein. Docking virtual screening was performed for both the synthesized and reference molecules. Free binding energy (ΔG) results are included in Table 3 which represents the most stability fitting of the ligands inside biomolecular system.

Exploring our results in further details, the free binding energy of each cluster rank integrated in a vertical bar chart for the simulated synthesized molecule and the comparable reference inhibitors as shown in Fig. 9. ΔG after each cluster con-

tributes the negative column area for K36 inhibitor where it reached the validated optimized free binding energy at cluster of −7.67 kcal/mol while CT-complex contributes some of negatively ΔG values compared with k36 and rotatory reach to lowest energy value −5.65 kcal/mol. In case of UXS reference inhibitor, the lowest ΔG value is −9.59 kcal/mol and this energy is strong compared with k36, while the lowest ΔG of CT-complex reached to −8.01 kcal/mol and also is higher than of CT-complex binding in 6WTT. Further comparable results in 6XBH and 7JRN, showed that ΔG of the studied CT-complex is of values −4.73 kcal/mol and −3.17 kcal/mol in the two receptors, respectively.

3.4.9. Molecular dynamic (MD) simulation analysis

Stability of the ligand inside the protein cleft active site is mainly time-dependent in considering the variables and statistical parameters [49,50]. MD simulation can evaluate this stability strength in the desired target. This type of simulation was performed using Chimera software where the ligand-free receptor was first prepared by missing hydrogen addition, charge adjustment on the whole macromolecular chain, and then solvation through certain dimensions as shown in Fig. 10 for 6WTT, 6XA4, 6XBH, and

7JRN protein targets. The steepest descent steps were chosen till 100 with size 0.02 Å. The conjugate gradient steps were 10 also with size 0.02 Å. Root mean square deviation (RMSD) value is a time-dependent expression for ligand-protein stabilization model. RMSD is an important parameter in detecting and analyzing the equilibration followed by producing MD trajectories. RMSD frames and their potential energy were plotted against time (fs) as shown in Fig. 11 RMSD specific range describes the stability of MD trajectory for a time. Increasing the period time with a relatively constant RMSD increases the binding affinity of the ligand-protein domain. With fastening in frame numbers, the potential energy decreases and then RMSD mostly decrease till reaches to relatively smooth and constant plot at higher frames.

During analysis of MD simulation, estimation of the potential energy is an indicator of the system path stability. In binding CT-complex with 6WTT and 6XA4 domains, the potential energy decreases with time, resulting in a decrease in RMSD at higher frames. As mentioned, in previous work [51], the values of RMSD less than 3 Å are considered in the docking fit protocol and accurate scanning around stability ranges towards the binding pose. At frames 1- 200, RMSD in 6WTT decreased from 3.441 to 1.553) and in 6XA4 the value increased from 1 to 150 then decreased again reaching frames number 200. Otherwise, 6XBH and 7JRN bound systems show higher potential energy with increasing RMSD and effect the stabilization and binding affinity. Furthermore, RMSD mapping in the docking pose for both protein and ligand frames refine the docking protocol. As shown in Fig. 12 2D map was established in the range of 1.3 Å – 3.0 Å for all interacted ligand-receptors molecular poses and it was found that the fitting with RMSD < 1.5 take the map majority (white color code) while the RMSD > 1.5 take the map minority (black color code). Analyzing the mapping areas, CT-complex bound with 6WTT and 6XA4 show RMSD mostly emphasis as small values white contributes.

Summarizing the following results, according to the free binding energy and comparative RMSD cutoff-potential energy variation, it was predicted that the synthesized CT-complex could bind with 6XA4 then 6WTT targets in a higher score values better than in case of 6ABH and 7JRN active viral receptors.

4. Conclusion

A new charge-transfer complex was prepared between a Schiff base 2-((2-hydroxybenzylidene) amino)−2-(hydroxymethyl) propane-1,3-diol [SAL-THAM] as e-donor and chloranilic acid (CLA) as e-acceptor. The prepared CT complex [CLA-SAL-THAM] has been studied experimentally and theoretically. The elemental analysis of the solid CT complex proved its formation in 1:1 (donor: acceptor) similar to that in solution. Relying on the Infrared spectral feature, the new complex was suggested to contain hydrogen bonds beside charge-transfer interactions. The molecular composition of the complex was estimated using Job's photometric method and was found to be 1:1 in all the used solvents. The formation constant was determined in methanol, ethanol and acetonitrile. The highest value was verified in acetonitrile and the smallest one in methanol, approving the produced complex's high stability in the aprotic solvent.

The geometrical optimization of the expected structure of the formed complex supported H- bonding. The computational electronic spectra showed that the charge transfer mainly was assigned and contributed from HOMO-1 to LUMO. MEP study revealed SAL-THAM as electron donor, and CLA is described as an electron acceptor, which was the origin of H-bond formation. Molecular docking was applied to identify the potent activity of the titled complex towards different types of genome SARS-CoV-2 protease acceptors (M^{pro} and PL^{pro}). The docking results predicted a high binding affinity to the COVID-19 protease. They can inhibit its viral infec-

tion by blocking several active amino acid sides compared to the previously occurred standard ligands. Free binding energy evaluated higher ligand path stability for M^{Pro} such 6XA4 then 6WTT domains while predicted a weak score towards 64BH and PL^{Pro} -7JRN target. The results were validated and refined through molecular dynamic simulation analysis and exploring RMSD parameter values depending on the time of trajectory stability.

Declaration of Competing Interest

The authors declare that they have no known competing financial interests or personal relationships that could have appeared to influence the work reported in this paper.

Supplementary materials

Supplementary material associated with this article can be found, in the online version, at doi:10.1016/j.molstruc.2021.132010.

CRediT authorship contribution statement

Tarek E. Khalil: Supervision, Conceptualization, Methodology, Visualization, Investigation, Writing – original draft, Writing – review & editing. **Hemmat A. Elbadawy:** Conceptualization, Methodology, Visualization, Investigation, Writing – review & editing. **Asmaa A. Attia:** Visualization, Methodology, Writing – original draft. **Doaa S. El-Sayed:** Formal analysis, Software, Methodology, Visualization, Writing – review & editing.

References

[1] M. Baseer, V. Jadhav, R. Phule, Y. Archana, Y. Vibhute, Synthesis and antibacterial activity of some new Schiff bases, Orient. J. Chem. 16 (2000) 553–556.

[2] J. Somwanshi, Synthesis and characterization of biologically active schiff's bases derived from trimethoprim, J. Glob. Biosci. 9 (2020) 6963–6973 www.mutagens.co.in/jgb/vol.09/04/090404.

[3] S. Ren, R. Wang, K. Komatsu, P. Bonaz-Krause, Y. Zyrianov, C.E. McKenna, C. Csipke, Z.A. Tokes, E.J. Lien, Synthesis, biological evaluation, and quantitative structure− activity relationship analysis of new Schiff bases of hydroxysemicarbazide as potential antitumor agents, J Med. Chem. 45 (2002) 410–419, doi:10.1021/jm010252q.

[4] C.M. Delpiccolo, E.G. Mata, Stereoselective solid-phase synthesis of 3, 4-substituted azetidinones as key intermediates for mono-and multicyclic β-lactam antibiotics and enzyme inhibitors, Tetrahedron Asymmetry 13 (2002) 905–910, doi:10.1016/S09574166(02)00214-8.

[5] P. Przybylski, A. Huczynski, K. Pyta, B. Brzezinski, F. Bartl, Biological properties of Schiff bases and azo derivatives of phenols, Curr. Org. Chem. 13 (2009) 124–148, doi:10.2174/138527209787193774.

[6] A.O.d. Souza, F. Galetti, C.L. Silva, B. Bicalho, M.M. Parma, S.F. Fonseca, A.J. Marsaioli, A.C. Trindade, R.P.F. Gil, F.S. Bezerra, Antimycobacterial and cytotoxicity activity of synthetic and natural compounds, Quím. Nova 30 (2007) 1563–1566, doi:10.1590/S0100-40422007000700012.

[7] L. Androš Dubraja, K. Molčanov, D. Žilić, B. Kojić-Prodić, E. Wenger, Multifunctionality and size of the chloranilate ligand define the topology of transition metal coordination polymers, New J. Chem. 41 (2017) 6785–6794, doi:10.1039/C7NJ01058C.

[8] K.M. Al-Ahmary, M.M. Habeeb, S.H. Aljahdali, Synthesis, spectroscopic studies and DFT/TD-DFT/PCM calculations of molecular structure, spectroscopic characterization and NBO of charge transfer complex between 5-amino-1, 3-dimethylpyrazole (5-ADMP) with chloranilic acid (CLA) in different solvents, J. Mol. Liq. 277 (2019) 453–470, doi:10.1016/j.molliq.2018.12.072.

[9] K.M. Al-Ahmary, M.M. Habeeb, A.H. Al-Obidan, Charge transfer complex between 2, 3-diaminopyridine with chloranilic acid. Synthesis, characterization and DFT, TD-DFT computational studies, Spectrochim. Acta Part A 196 (2018) 247–255, doi:10.1016/j.saa.2018.02.025.

[10] R.M. Alghanmi, S.M. Soliman, M.T. Basha, M.M. Habeeb, Electronic spectral studies and DFT computational analysis of hydrogen bonded charge transfer complexes between chloranilic acid and 2, 5-dihydroxy-p-benzoquinone with 2-amino-4-methylbenzothiazole in methanol, J. Mol. Liq. 256 (2018) 433–444, doi:10.1016/j.molliq.2018.02.056.

[11] I.V. Kuvykin, V.V. Ptushenko, A.V. Vershubskii, A.N. Tikhonov, Regulation of electron transport in C3 plant chloroplasts in situ and in silico: short-term effects of atmospheric CO_2 and O_2, Biochim. Biophys. Acta (BBA) Bioenerg. 1807 (2011) 336–347, doi:10.1016/j.bbabio.2010.12.012.

[12] H. Ozawa, T. Hino, T. Ohtsu, K. Wada, K. Tanaka, A new type of electrochemical oxidation of alcohols mediated with a ruthenium–dioxolene–amine complex in neutral water, Inorg. Chim. Acta 366 (2011) 298–302, doi:10.1016/j.ica.2010.11.013.

[13] H. Salem, Spectrophotometric determination of β-adrenergic blocking agents in pharmaceutical formulations, J. Pharm. Biomed. Anal. 29 (2002) 527–538, doi:10.1016/S0731-7085(02)00100-0.

[14] I.M. Khan, A. Ahmad, Synthesis, spectral and thermal studies of the newly hydrogen bonded charge transfer complex of o-phenylenediamine with π acceptor picric acid, Spectrochim. Acta Part A 77 (2010) 437–441, doi:10.1016/j.saa.2010.06.011.

[15] R.D. Jiang, M.Q. Liu, Y. Chen, C. Shan, Y.W. Zhou, X.R. Shen, Q. Li, L. Zhang, Y. Zhu, H.R. Si, Pathogenesis of SARS-CoV-2 in transgenic mice expressing human angiotensin-converting enzyme 2, Cell 182 (2020) 50–58 e58, doi:10.1016/j.cell.2020.05.027.

[16] R. Lu, X. Zhao, J. Li, P. Niu, B. Yang, H. Wu, W. Wang, H. Song, B. Huang, N. Zhu, Genomic characterisation and epidemiology of 2019 novel coronavirus: implications for virus origins and receptor binding, Lancet 395 (2020) 565–574, doi:10.1016/S0140-6736(20)30251-8.

[17] F. Wu, S. Zhao, B. Yu, Y.M. Chen, W. Wang, Z.G. Song, Y. Hu, Z.W. Tao, J.H. Tian, Y.Y. Pei, A new coronavirus associated with human respiratory disease in China, Nature 579 (2020) 265–269, doi:10.1038/s41586-020-2008-3.

[18] C. Huang, Y. Wang, X. Li, L. Ren, J. Zhao, Y. Hu, L. Zhang, G. Fan, J. Xu, X. Gu, Clinical features of patients infected with 2019 novel coronavirus in Wuhan, China, lancet 395 (2020) 497–506, doi:10.1016/S0140-6736(20)30183-5.

[19] S. Xia, M. Liu, C. Wang, W. Xu, Q. Lan, S. Feng, F. Qi, L. Bao, L. Du, S. Liu, Inhibition of SARS-CoV-2 (previously 2019-nCoV) infection by a highly potent pan-coronavirus fusion inhibitor targeting its spike protein that harbors a high capacity to mediate membrane fusion, Cell Res. 30 (2020) 343–355, doi:10.1038/s41422-020-0305-x.

[20] B. Robson, Computers and viral diseases. Preliminary bioinformatics studies on the design of a synthetic vaccine and a preventative peptidomimetic antagonist against the SARS-CoV-2 (2019-nCoV, COVID-19) coronavirus, Comput. Biol. Med. 119 (2020) 103670, doi:10.1016/j.compbiomed.2020.103670.

[21] B. Robson, COVID-19 Coronavirus spike protein analysis for synthetic vaccines, a peptidomimetic antagonist, and therapeutic drugs, and analysis of a proposed achilles' heel conserved region to minimize probability of escape mutations and drug resistance, Comput. Biol. Med. 121 (2020) 103749, doi:10.1016/j.compbiomed.2020.103749.

[22] S. Jeon, M. Ko, J. Lee, I. Choi, S.Y. Byun, S. Park, D. Shum, S. Kim, Identification of antiviral drug candidates against SARS-CoV-2 from FDA-approved drugs, Antimicrob. Agents Chemother. 64 (7) (2020) e00819–e00820, doi:10.1128/AAC.00819-20.

[23] S. Aherfi, B. Pradines, C. Devaux, S. Honore, P. Colson, B.L. Scola, D. Raoult, Drug repurposing against SARS-CoV-1, SARS-CoV-2 and MERS-CoV, Fut. Microbiol. 16 (17) (2021) 1341–1370, doi:10.2217/fmb-2021-0019.

[24] I. Khater, A. Nassar, In silico molecular docking analysis for repurposing approved antiviral drugs against SARS-CoV-2 main protease, Biochem. Biophys. Rep. 27 (2021) 101032, doi:10.1016/j.bbrep.2021.101032.

[25] W.D. Jang, S. Jeon, S. Kim, S.Y. Lee, Drugs repurposed for COVID-19 by virtual screening of 6,218 drugs and cell-based assay, PNAS 118 (30) (2021) e2024302118, doi:10.1073/pnas.2024302118.

[26] Y. Zhou, Y. Hou, J. Shen, Y. Huang, W. Martin, F. Cheng, Network-based drug repurposing for novel coronavirus 2019-nCoV/SARS-CoV-2, Cell Discov. 6 (2020) 1–18, doi:10.1038/s41421-020-0153-3.

[27] R. Shetty, A. Ghosh, S.G. Honavar, P. Khamar, S. Sethu, Therapeutic opportunities to manage COVID-19/SARS-CoV-2 infection: present and future, Indian J. Ophthalmol. 68 (2020) 693–702 10.4103%2Fijo.IJO_639_20.

[28] C. Liu, Q. Zhou, Y. Li, L.V. Garner, S.P. Watkins, L.J. Carter, J. Smoot, A.C. Gregg, A.D. Daniels, S. Jervey, Research and development on therapeutic agents and vaccines for COVID-19 and related human coronavirus diseases, ACS Cent. Sci. 6 (2020) 315–331, doi:10.1021/acscentsci.0c00272.

[29] F. Cheng, In silico oncology drug repositioning and polypharmacology, Cancer Bioinform. (2019) 243–261, doi:10.1007/978-1-4939-8868-6_15.

[32] B.H. Harcourt, D. Jukneliene, A. Kanjanahaluethai, J. Bechill, K.M. Severson, C.M. Smith, P.A. Rota, S.C. Baker, Identification of severe acute respiratory syndrome coronavirus replicase products and characterization of papainlike protease activity, J. Virol. 78 (2004) 13600–13612, doi:10.1128/JVI.78.24.13600-13612.2004.

[31] K. Lim, L.F. Ng, D. Liu, Identification of a novel cleavage activity of the first papain-like proteinase domain encoded by open reading frame 1a of the coronavirus Avian infectious bronchitis virus and characterization of the cleavage products, J. Virol. 74 (2000) 1674–1685, doi:10.1128/JVI.74.4.1674-1685.2000.

[30] C. Liu, Y. Ma, J. Zhao, R. Nussinov, Y.C. Zhang, F. Cheng, Z.K. Zhang, Computational network biology: data, models, and applications, Phys. Rep. 846 (2020) 1–66, doi:10.1016/j.physrep.2019.12.004.

[33] W. Vuong, M.B. Khan, C. Fischer, E. Arutyunova, T. Lamer, J. Shields, H.A. Saffran, R.T. McKay, M.J. van Belkum, M.A. Joyce, H.S. Young, D.L. Tyrrell, J.C. Vederas, M.J. Lemieux, Feline coronavirus drug inhibits the main protease of SARS-CoV-2 and blocks virus replication, Nat. Commun. 11 (2020) 4282, doi:10.1038/s41467-020-18096-2.

[34] S.M. Lee, K.S. Sim, K.M. Lo, Synthesis, characterization and biological studies of diorganotin(IV) complexes with tris[(hydroxymethyl)aminomethane] Schiff bases, Inorg. Chim. Acta 429 (2015) 195–208, doi:10.1016/j.ica.2015.01.017.

[35] A. Goel, V.J. Ram, Natural and synthetic 2H-pyran-2-ones and their versatility in organic synthesis, Tetrahedron 65 (2009) 7865–7913.

[36] M. Frisch, G. Trucks, H. Schlegel, G. Scuseria, M. Robb, J. Cheeseman, G. Scalmani, V. Barone, G. Petersson, H. Nakatsuji, Gaussian Development Version, Revision I. 13, Gaussian, Inc, Wallingford, CT, 2016.

[37] A. Gómez Marigliano, E. Varetti, Self-association of formamide in carbon tetrachloride solutions: an experimental and quantum chemistry vibrational and thermodynamic study, J. Phys. Chem. A 106 (2002) 1100–1106, doi:10.1021/jp011060.

[38] Y. Takano, K. Houk, Benchmarking the conductor-like polarizable continuum model (CPCM) for aqueous solvation free energies of neutral and ionic organic molecules, J. Chem. Theor. Comput. 1 (2005) 70–77, doi:10.1021/ct049977a.

[39] M. Cossi, N. Rega, G. Scalmani, V. Barone, Energies, structures, and electronic properties of molecules in solution with the C-PCM solvation model, J. Comput.Chem. 24 (2003) 669–681, doi:10.1002/jcc.10189.

[40] H.J. Wörner, C.A. Arrell, N. Banerji, A. Cannizzo, M. Chergui, A.K. Das, P. Hamm, U. Keller, P.M. Kraus, E. Liberatore, Charge migration and charge transfer in molecular systems, Struct. Dynam. 4 (2017) 061508, doi:10.1063/1.4996505.

[41] G.M. Morris, R. Huey, W. Lindstrom, M.F. Sanner, R.K. Belew, D.S. Goodsell, A.J. Olson, Autodock4 and AutoDockTools4: automated docking with selective receptor flexiblity, J. Comput. Chem. 16 (2009) 2785–2791.

[42] E.F. Pettersen, T.D. Goddard, C.C. Huang, G.S. Couch, D.M. Greenblatt, E.C. Meng, T.E. Ferrin, UCSF chimera – a visualization system for exploratory research and analysis, J. Comput. Chem. 25 (2004) 1605–1612, doi:10.1002/jcc.20084.

[43] A. El-Dissouky, T.E. Khalil, H.A. Elbadawy, D.S. El-Sayed, A.A. Attia, S. Foro, X-ray crystal structure, spectroscopic and DFT computational studies of H-bonded charge transfer complexes of tris (hydroxymethyl)aminomethane (THAM) with chloranilic acid (CLA), J. Mol. Struct. 1200 (2020) 127066, doi:10.1016/j.molstruc.2019.127066.

[44] A. Airinei, M. Homociano, D.O. Dorohoi, Changes induced by solvent polarity in electronic absorption spectra of some azo disperse dyes, J. Mol. Liq. 157 (2010) 13–17, doi:10.1016/j.molliq.2010.07.011.

[45] D.O.N. Gardner, L. von Szentpály, Valence state atoms in molecules. 5. Universal scaling of the inner branch of fifty RKR potential energy curves. Comparison of the valence state, Morse, and Rydberg curves, J. Phys.Chem. A 103 (1999) 9313–9322, doi:10.1021/jp991864d.

[46] D.W. Lim, S. Sadakiyo, H. Kitagawa, Proton transfer in hydrogen-bonded degenerate systems of water and ammonia in metal–organic frameworks, Chem. Sci. 10 (2019) 16–33, doi:10.1039/C8SC04475A.

[47] N.S. Venkataramanan, A. Suvitha, Y. Kawazoe, Unravelling the nature of binding of cubane and substituted cubanes within cucurbiturils: a DFT and NCI study, J. Mol. Liq. 260 (2018) 18–29, doi:10.1016/j.molliq.2018.03.071.

[48] X. Gao, B. Qin, P. Chen, K. Zhu, P. Hou, J.A. Wojdyla, M. Wang, S. Cui, Crystal structure of SARS-CoV-2 papain-like protease, Acta Pharm. Sin. B 11 (2021) 237–245, doi:10.1016/j.apsb.2020.08.014.

[49] A. Hospital, J.R. Goñi, M. Orozco, J.L. Gelpí, Molecular dynamics simulations: advances and applications, Adv. Appl. Bioinforma. Chem. 8 (2015) 37–47.

[50] S.T. Ngo, N.M. Tam, M.Q. Pham, T.H. Nguyen, Benchmark of popular free energy approaches revealing the inhibitors binding to SARS-CoV-2 mpro, J. Chem. Info. Mod. 61 (5) (2021) 2302–2312, doi:10.1021/acs.jcim.1c00159.

[51] G. Duan, C. Ji, J.Z.H. Zhang, Developing an effective polarizable bond method for small molecules with application to optimized molecular docking, RSC Adv. 10 (2020) 15530–15540, doi:10.1039/D0RA01483D.